Collaborative Coupled Hyperspectral Unmixing based Sub-Pixel Change Detection for Analyzing Coastal Wetlands

Minghui Chang, Xiangchao Meng, *Member, IEEE,* Weiwei Sun, *Senior Member, IEEE,* Gang Yang, *Member, IEEE,* Jiangtao Peng, *Senior Member, IEEE*

***Abstract*—Owing to the complicated and heterogeneous distribution characteristics of wetland features, the existing hyperspectral technology is difficult to investigate the inner-pixel subtle changes. In this paper, we present a sub-pixel change detection method based on collaborative coupled unmixing (SCDUM) for monitoring coastal wetlands. A novel multitemporal and spatial scale collaborative endmember extraction method based on joint spatial and spectral information is proposed. In the proposed method, the multitemporal hyperspectral images are firstly jointly clustered and segmented based on multi-feature fusion of spectral features, texture features, and shape features. Then a different spatial scale non-negative matrix factorization based on original and down-sampled multitemporal hyperspectral images is proposed to accurately extract the pure endmembers of each segmented images. Finally, the global abundance of the multitemporal image is effectively estimated for change detection. In addition, in order to verify the accuracy of the change detection results without reference, an accuracy verification strategy by using high spatial resolution Sentinel-2A image as auxiliary data is implemented. The Yellow River Estuary coastal wetlands was selected as the research area, and the Gaofen (GF)-5 and ZY-1 02D hyperspectral images were used as the research data. In particular, the proposed method not only provides the overall change information, but also obtains the component of change direction and intensity of each kind of endmember, and the experimental results shows that the SCDUM gives more accurate detection results, with closer to the endmember spectral curves of real objects, compared with other state-of-the-art methods.**

***Index Terms*—Hyperspectral remote sensing, change detection, spectral unmixing, sub-pixel**

This work was supported by the National Natural Science Foundation of China under Grant 41971296, Grant 41801256, Grant 61871177, Grant 41801252, in part by the Zhejiang Provincial Natural Science Foundation of China under Grant LR19D010001, the fellowship of China Postdoctoral Science Foundation under Grant 2020M672490, and in part by the K. C. Wong Magna Fund in Ningbo University. (*Corresponding author: Xiangchao Meng; Weiwei Sun*)

Minghui Chang, Weiwei Sun, and Gang Yang, are with the Department of Geography and Spatial Information Techniques, Ningbo University, Ningbo 315211, China (e-mail: 1513385339@qq.com; sunweiwei@nbu.edu.cn; yanggang@nbu.edu.cn;).

Xiangchao Meng is with the Faculty of Electrical Engineering and Computer Science, Ningbo University, Ningbo 315211, China (e-mail: mengxiangchao@nbu.edu.cn)

J. Peng is with the Hubei Key Laboratory of Applied Mathematics, Faculty of Mathematics and Statistics, Hubei University, Wuhan 430062, China (e-mail: pengjt1982@hubu.edu.cn).

I. Introduction

Coastal wetlands has rich water and biological resources, and play an important role in protecting biodiversity, and regulating local climate [1, 2]. In particular, the Yellow River Delta, located on the west bank of the Pacific Ocean, has one of the most complete, extensive, and youngest coastal wetlands ecosystems in China [3]. Unfortunately, in recent years, the ecosystem of the Yellow River estuary wetlands has been severely damaged, and the inter-annual changes have been obvious. Hyperspectral remote sensing can collect abundant spectral information from visible to shortwave infrared wavelength ranging from 0.4 to 2.5 μm, and offer more detailed subtle information on spectral changes in multitemporal scenes [4, 5].

An effective change detection monitoring using hyperspectral remote sensing is important and urgent for the protection of the Yellow River estuary wetlands. Current change detection methods are mainly divided into two categories: pixel-based methods and sub-pixel-based methods. Image algebra (IA), change vector analysis (CVA), image transformation method, and classification-based methods belong to pixel-based change detection methods [6]. The IA method is the earliest change detection method [7]. It detects the changes of ground objects by calculating the band algebra between multi-temporal images. The typical methods mainly include as follows: difference method, ratio method and image regression method. Change vector analysis is an extension of the IA [8]. The representative methods include kernel change detection method and probability space change vector analysis method [9]. Image transformation method (IT) improves the accuracy of change detection by extracting features from image bands, and iterated principal component analysis (ITPCA) [10], iterative reweighted multivariate alteration detection (IRMAD) [11], and so on [12]. At the same time, the classification-based methods can detect the change of bi-temporal classified images, such as post classification change detection method and joint classification change detection method [13]. Although the above pixel-based methods obtain good results, it is difficult to get subtle and potential change information from pixel-based change results directly. To solve this problem, many researchers have conducted research on sub-pixel based change detection methods. The current sub-pixel change detection methods mainly originate from the idea of image unmixing .

Du et al. [14] firstly proposed a general framework for changing detection based on spectral unmixing in 2013. This method focuses on urban land-cover change via exploring

inner-pixel subtle changes, not only achieves the binary change detection map, but also provides the characterization about change direction and intensity simultaneously. Hsieh et al. [15] studied specific cases by using a sub-pixel change detection method based on unmixing. The sub-pixel change detection for landslide spreading is realized by combining slope characteristics and abundance information obtained from unmixing. In recent years, the research on sub-pixel change detection has continued. Ertürk et al. [16] proposed sparse unmixing based sub-pixel change detection method in 2016. It reveals the subpixel level changes which occur in a multitemporal series through sparse unmixing, and dictionary pruning is exploited for the first time in hyperspectral change detection. Liu et al. [17] proposed an unsupervised multi-temporal spectral unmixing detection method. In this method, the multi temporal endmembers are extracted in the multitemporal domain of hyperspectral images, and the endmembers are recognized according to the proposed change analysis strategy. Finally, the contribution of change endmember abundance to pixels is analyzed to complete the change detection. The results of above sub-pixel change analysis based on spectral unmixing largely depend on the accuracy of endmember extraction. However, different from the regular distribution of urban features, wetland features are very complicated, and so applying the conventional change detection based on sub-pixel directly into wetland area has great limitations. 1) The coastal wetland's ecosystem is complicated and high fragmentation of ground objects, and therefore it is difficult to guarantee good endmember extraction results. For example, potholes and Culture Pond, tamarisk and suaeda salsa (the spectral separation between vegetation and water is very small) are difficult to be identified from each other. 2) the existing change analysis based on sub-pixels is lack of actual verification, and the change results without reference in practical applications should also be considered.

In the paper, we proposed a sub-pixel change detection method based on collaborative coupled unmixing (SCDUM) for coastal wetlands based on hyperspectral images. First, a novel multitemporal and spatial scale collaborative endmember extraction method is proposed, and the multitemporal abundance estimation is implemented to obtain the abundances of main ground objects at different phases. Then, the change map of each endmember is calculated, and the overall change map is obtained by summarizing all the endmember change maps. In order to verify the accuracy of the method, we innovative presented a change detection accuracy verification strategy, by using high spatial resolution images as the auxiliary data.

The main contributions of this paper include:

1) We proposed a collaborative coupled unmixing based hyperspectral sub-pixel change detection method for analyzing coastal wetlands. A novel multitemporal and spatial scale collaborative unmixing method based on joint spatial and spectral information is proposed, and the change detection for the complicated coastal wetlands can be effectively estimated.

2) We implemented a sub-pixel change detection accuracy verification strategy in the real applications without reference. In the case that the real land cover change is unknown, we can get the change of the ground objects through the high spatial resolution of different time phases (the same period with the hyperspectral image). The higher the corresponding spatial resolution is, the smaller the error is.

3) To the best of our knowledge, this is the first study aimed at detecting the interannual change of the Yellow River Estuary by sub-pixel analysis using the satellite borne hyperspectral image data of China. The method is not only suitable for the Yellow River Estuary, but also can be applied to other wetlands or complicated surface areas.

The structure of this paper is organized as follows. The proposed method of change detection and accuracy verification is specifically described in Section II. The experimental results and analysis are presented in Section III. The discussion is given in Section IV. The conclusion is shown in Section V .

II. Methodology

2.1 The idea of SCDUM

Fig. 1 shows the proposed hyperspectral sub-pixel change detection method SCDUM, which consists of two parts: multitemporal image unmixing and change detection. For the spectral unmixing, a novel collaborative coupled unmixing method for different phase images is proposed. First, multi-temporal images are preprocessed by orthorectification, radiometric calibration, atmospheric correction, image registration, and image mosaic. Second, the processed multi-temporal images are collaboratively clustered and segmented by comprehensively considering spectral features, texture features, and shape features. Then, a down-sampling operation is performed for each segmented image, and the down-sampled and original multi-temporal images are collaboratively unmixed by different spatial scale nonnegative matrix factorization (DSNMF) to more accurately extract endmembers. The sparse unmixing by variable splitting and augmented Lagrangian (SUNSAL) [18] is finally adopted to estimate the multi-temporal abundances, and the change detection results are obtained via abundance subtraction.

In the following section, we use bold uppercase to represent matrices (e.g., Z) and lowercase letters to express vectors (e.g., z). t1 and t2 represent the images of the first and second phases respectively. $\mathbf{HS}^{T_{1,2}}$ indicates the segmented hyperspectral image, and $\mathbf{HS}_L^{T_{1,2}}$ represents the low-resolution segmented hyperspectral image after down-sampling.

2.2 DSNMF

In this section, the DSNMF method based on joint spatial and spectral information is proposed to extract accurate endmembers from coastal wetlands. It consists of three parts: 1) Multitemporal image clustering and segmentation using the spectral-geometric-texture collaborative information; 2) Endmember extraction using DSNMF on the segmented multitemporal images; and 3) Multitemporal abundance estimation.

This article has been accepted for publication in a future issue of this journal, but has not been fully edited. Content may change prior to final publication. Citation information: DOI 10.1109/JSTARS.2021.3104164, IEEE Journal of Selected Topics in Applied Earth Observations and Remote Sensing

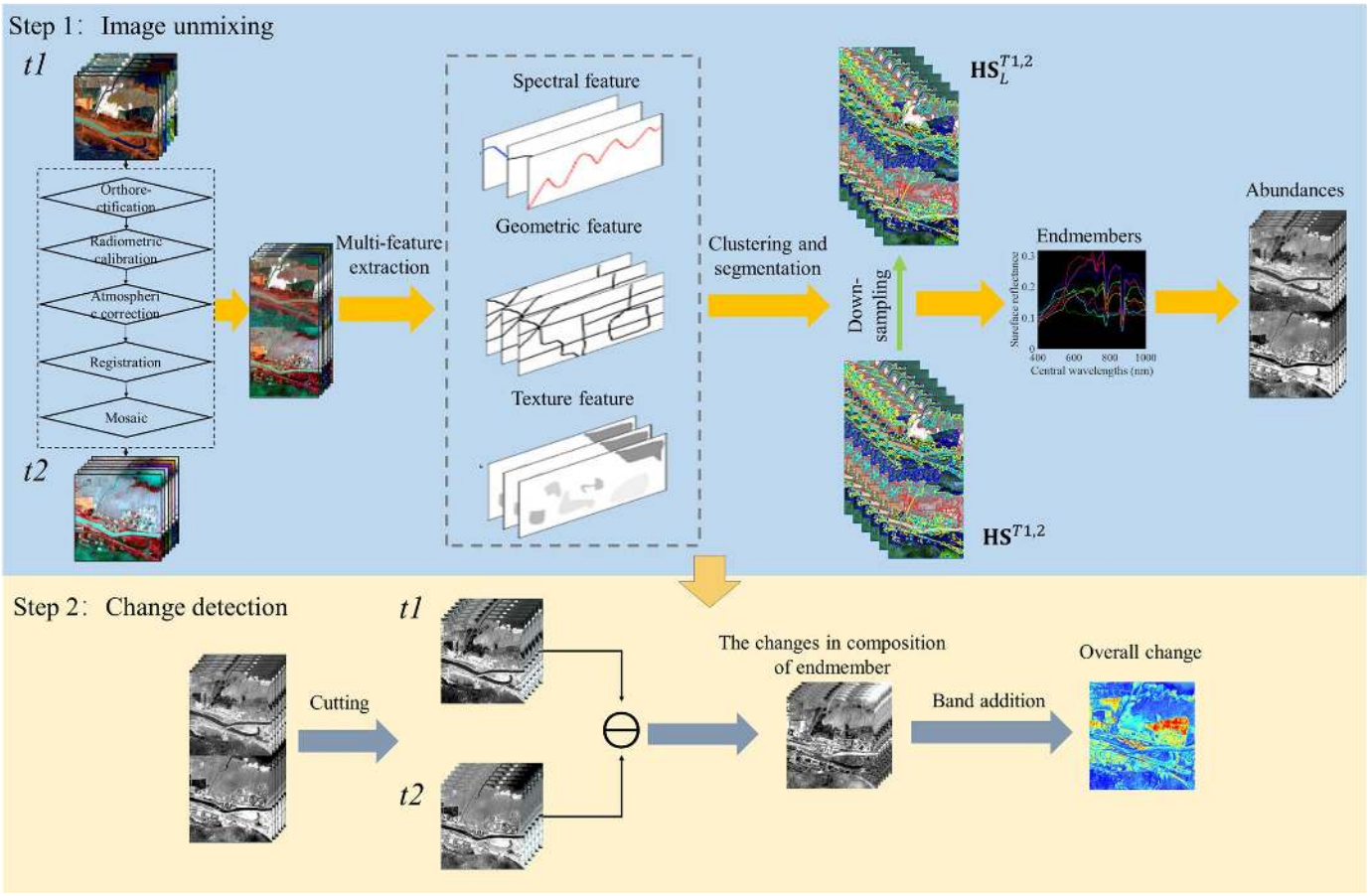

Fig. 1. The flowchart of the SCDUM method

A. *Spectral-Geometric-Texture collaborative clustering on multitemporal hyperspectral images*

An unsupervised clustering and segmentation for the mosaiced multitemporal images is performed by combining spectral, geometric and texture features. For the spectral features, principal component analysis (PCA) is carried out, and the first five principal components are selected as spectral features, which reduce the influence of noise on clustering to a certain extent [19]. For the texture features, the Local Binary Pattern (LBP) is used, due to its significant advantages of rotation invariance and gray invariance [20]. The specific formula of LBP is as follows:

$$LBP_{P,R} = \sum_{p=0}^{p-1} s(g_p - g_c)2^p \tag{1}$$

where $LBP_{P,R}$ is a local binary pattern; R is the radius; P is the number of neighboring pixels; g_p is the gray value of neighboring pixels; g_c is the gray value of the center pixel; $S(x)$ is the binary expression of gray level.

$$S(x) = \begin{cases} 1, & if\ \mathrm{x} \geq 0 \\ 0, & else \end{cases} \tag{2}$$

The canny operator can greatly reduce the false edges caused by noise, and it is generally better than Sobel, Roberts, Prewitt and other operators. Therefore, the canny operator is used to extract the edge information of the ground objects in coastal wetlands as a geometric feature [21].

After the above operations are completed, we superimpose the spectral features, geometric features, and texture features, and use K-means to cluster and segment the stacked multiple features.

B. Endmember extraction using DSNMF on segmented multitemporal images

Most of endmember extracting methods implement on spectral information, and that is insufficient for discriminating ground objects with small spectral divergences. For example, the same ground objects may show different spectral features affected by the surrounding ground objects, which usually results in the incorrect extraction of multiple endmembers on the same ground object. In this paper, we propose a DSNMF algorithm to extract pure endmembers from coastal wetlands hyperspectral images.

Using the segmented stacked multitemporal hyperspectral images, the different spatial scale coupled endmember extraction is performed on each segmented area. It is assumed that if an extracted endmember is pure in both original and spatially degraded (i.e., lower spatial resolution) hyperspectral images in the same spatial area, it is more truly a pure endmember. As shown in Fig.2, in our proposed method, the clustered and segmented image of mosaic hyperspectral image is spatially blurring using the Gaussian filter and down-sampling. The size of the blur kernel is 3×3, and the down-sampling factor is 3. Here, we define the Gaussian filter

This article has been accepted for publication in a future issue of this journal, but has not been fully edited. Content may change prior to final publication. Citation information: DOI 10.1109/JSTARS.2021.3104164, IEEE Journal of Selected Topics in Applied Earth Observations and Remote Sensing

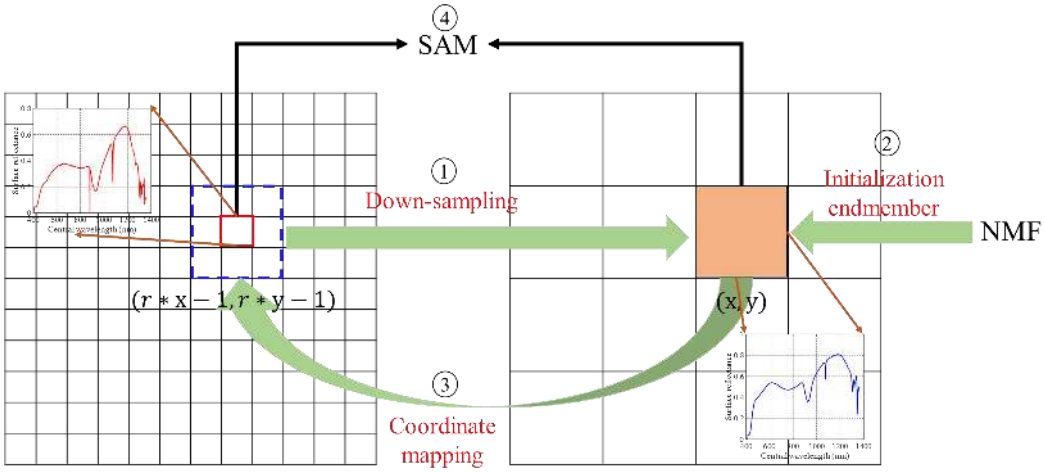

Fig. 2. An illustration of the proposed DSNMF.

and down-sampling operation as spatially degraded matrix $\mathbf{R}$, thus

$$\mathbf{HS}_{\omega L}^{t1,2} = \mathbf{R} \times \mathbf{HS}_{\omega}^{t1,2}, \quad \omega = [\mathbf{1}, \mathbf{2}, \cdots, nn] \tag{3}$$

where $\mathbf{HS}_{\omega}^{t1,2}$ is the $\omega - th$ clustered and segmented image of mosaic hyperspectral images, nn is the number of the segmented images, and the $\mathbf{HS}_{\omega_L}^{t1,2}$ is the spatially degraded image of the $\omega - th$ clustered and segmented image.

Using the linear spectral mixture model, the original and down-sampled hyperspectral images can be expressed as:

$$\mathbf{HS}_{\omega_L}^{t1,2} = \mathbf{E}_{\omega,m}\mathbf{A}_{\omega,m} + \mathbf{N}_{\omega,m} \tag{4}$$

where $\mathbf{E}_{\omega,m}$, $\mathbf{A}_{\omega,m}$ and $\mathbf{N}_{\omega,m}$ are respectively the endmember, abundance and the residual of the $\omega - th$ segmented down-sampled ones.

After that, the initial endmember in $\mathbf{HS}_{\omega_L}^{T1,2}$ is extracted through the NMF unmixing algorithm, represented as follows:

$$\begin{aligned} &\arg \min_{\mathbf{E}_{\omega,m},\ \mathbf{A}_{\omega,m}} \left\|\mathbf{HS}_{\omega_L}^{t1,2} - \mathbf{E}_{\omega,m}\mathbf{A}_{\omega,m}\right\|_F^2 \\ &s.t.\ \mathbf{A}_{\omega,m} > \mathbf{0};\ {\mathbf{A}_{\omega,m}}^T\mathbf{1} = \mathbf{1} \end{aligned} \tag{5}$$

where $\|\cdot\|_F^2$ is the Frobenius norm.

Using NMF unmixing algorithm to extract the endmembers of segmented images $\mathbf{HS}_{\omega_L}^{t1,2}$, $\mathbf{E}_{\omega,m}$ can be obtained, where $\mathbf{E}_{\omega,m} = [e_{\omega,m}^1, e_{\omega,m}^2, \cdots, e_{\omega,m}^j]$ ($\omega = [1,2,\cdots,nn]$) represents the endmember of the segmented images $\mathbf{HS}_{\omega_L}^{t1,2}$. Then, the coordinate mapping is performed to retrieve the pixel positions of the extracted endmembers $\mathbf{E}_{\omega} = [e_{\omega}^1, e_{\omega}^2, \cdots, e_{\omega}^j]$ ($\omega = [1,2,\cdots,nn]$) in the original image $\mathbf{HS}_{\omega}^{t1,2}$. For example, the position corresponding to the j-th endmember is:

$$x' = r * x - 1 \tag{6}$$

$$y' = r * y - 1 \tag{7}$$

where (x', y') are the spatial coordinates of the j-th endmember in the original image. $(x,\ y)$ are the corresponding spatial coordinates of the j-th endmember in the down-sampling low-resolution image. Finally, the spectral angle mapper (SAM) at the position of (x', y') and (x, y) is calculated to measure the spectral distance between the endmembers from the original and down-sampled hyperspectral images, and a threshold is set to determine whether the extracted endmembers are accurate. The specific operation is as follows:

$$\mathrm{SAM}\left(e_{\omega}^j, e_{\omega,m}^j\right) = \cos^{-1}\left(\frac{\langle e_{\omega}^j, e_{\omega,m}^j\rangle}{\left\|e_{\omega}^j\right\| \cdot \left\|e_{\omega,m}^j\right\|}\right) \tag{8}$$

$$Pure\ endmember = \begin{cases} yes,\ if\ \mathrm{SAM} < \varepsilon \\ no,\ else \end{cases} \tag{9}$$

where ε is the defined threshold. It is set to 0.1374 via cross-validation in our experiments.

All the clustered and segmented images are operated by using formulas (3)-(9), and these final endmembers are obtained:

$\mathbf{E}_m = [e_m^1,\ e_m^2, \cdots, e_m^j]$, $\mathbf{E} = [e^1,\ e^2,\ \cdots,\ e^j]$where $\mathbf{E}_m$ and $\mathbf{E}$ are the endmembers of $\mathbf{HS}_L^{t1,2}$ and $\mathbf{HS}^{t1,2}$ respectively.

Algorithm 1: DSNMF for endmember extraction

Input: The clustered and segmented hyperspectral images; Initial number of endmembers *j*; Number of iterations.

Output: Endmember spectrum

Define the number of clustered and segmented hyperspectral images *nn*, and the number of endmembers *n*.

$$\mathbf{HS}_{\omega_L}^{t1,2} = \mathbf{R} * \mathbf{HS}_{\omega}^{t1,2}, \quad \omega = [\mathbf{1}, \mathbf{2}, \cdots, nn]$$

$$\arg \min_{\mathbf{E}_{\omega,m},\ \mathbf{A}_{\omega,m}} \left\|\mathbf{HS}_{\omega_L}^{t1,2} - \mathbf{E}_{\omega,m}\mathbf{A}_{\omega,m}\right\|_F^2$$

$$s.t.\ \mathbf{A}_{\omega,m} > \mathbf{0};\ {\mathbf{A}_{\omega,m}}^T\mathbf{1} = \mathbf{1}$$

$\mathbf{E}_{\omega,m} = [e_{\omega,m}^1, e_{\omega,m}^2, \cdots, e_{\omega,m}^j]$, $\mathbf{E}_{\omega} = [e_{\omega}^1, e_{\omega}^2, \cdots, e_{\omega}^j]$

for ω =1:*nn*

  for *j* =1:*n*

$$e_{\omega,m}^j\ (x', y') = e_{\omega}^j(x, y)$$

$$x' = r * x - 1$$

$$y' = r * y - 1$$

$$e_{\omega}^j \in \mathbf{E}_{\omega},\ e_{\omega,m}^j \in \mathbf{E}_{\omega,m}$$

$$\mathrm{SAM}\left(e_{\omega}^j, e_{\omega,m}^j\right) = \cos^{-1}\left(\frac{\langle e_{\omega}^j, e_{\omega,m}^j\rangle}{\left\|e_{\omega}^j\right\| \cdot \left\|e_{\omega,m}^j\right\|}\right)$$

  if *SAM*< ε ***then***

    this is a pure endmember

  end

$\mathbf{E}_m = [e_m^1,\ e_m^2, \cdots, e_m^j]$, $\mathbf{E} = [e^1,\ e^2,\ \cdots,\ e^j]$

This article has been accepted for publication in a future issue of this journal, but has not been fully edited. Content may change prior to final publication. Citation information: DOI 10.1109/JSTARS.2021.3104164, IEEE Journal of Selected Topics in Applied Earth Observations and Remote Sensing

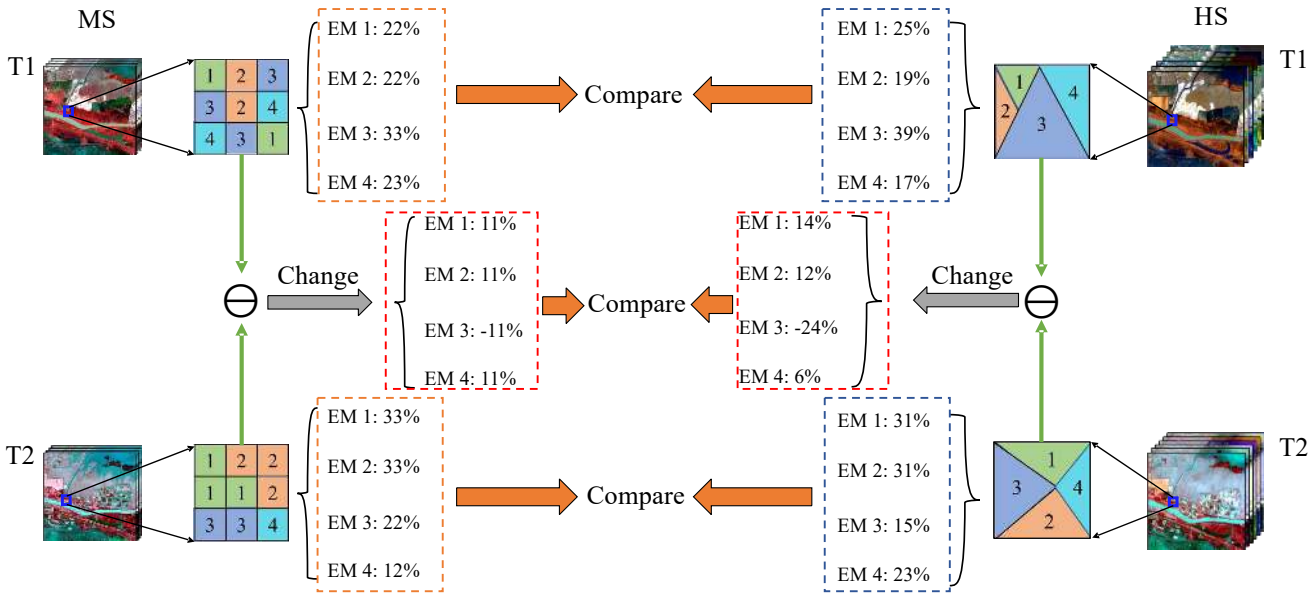

Fig. 3. Flowchart of the proposed accuracy verification method.

C. Multitemporal abundance estimation

The abundance estimation is devoted to calculate the proportion of endmembers in each pixel. Using the extracted endmember set, we estimate the endmember abundance on the mosaiced global image. There are many methods and these classical methods include sum-to-one constrained linear spectral unmixing (SCLSU) [22] and fully constrained least squares (FCLS) [23]. Recently, the abundance estimation algorithm SUNSAL [18] based on sparse expression has achieved excellent results. The SUNSAL is utilized, and it is represented as:

$$\min_{\mathbf{A}} \frac{1}{2}\|\mathbf{HS}^{T_{1,2}} - \mathbf{EA}\|_2^2 + \lambda\|\mathbf{A}\|_1 \quad s.t.\ \mathbf{A} \geq 0, \mathbf{A} = 1^{\mathrm{T}} \tag{10}$$

where $\mathbf{HS}^{T_{1,2}}$ is mosaiced image, and λ is the regularization parameter.

2.3 Change Detection

A. Sub-pixel change detection

As shown in step 2 of the Fig. 2, the abundance map of the mosaiced image is clipped to obtain the abundance maps at $t1$ and $t2$. Then, the change detection is estimated by subtracting the abundance maps at $t1$ and $t2$, represented as:

$$\mathbf{CD} = \mathbf{A}_{\mathrm{T2}} - \mathbf{A}_{\mathrm{T1}} \tag{11}$$

$$\mathbf{A}_{t1} = [a_{t1}^1, a_{t1}^2, \cdots, a_{t1}^j] \tag{12}$$

$$\mathbf{A}_{t2} = [a_{t2}^1, a_{t2}^2, \cdots, a_{t2}^j] \tag{13}$$

where $\mathbf{CD} = [\mathbf{cd}_1, \mathbf{cd}_2, \cdots, \mathbf{cd}_{\mathrm{j}}]$ are the difference images, $\mathbf{A}_{t1}$ represents the abundance map at $t1$, j is the number of endmembers, and $\mathbf{A}_{t2}$ represents the abundance map at $t2$.

The overall change is obtained from the summarization of composition changes from all the endmembers, represented as:

$$\mathbf{CD}_{overall} = |\mathbf{cd}_1| + |\mathbf{cd}_2| + \cdots + |\mathbf{cd}_j| \tag{14}$$

B. Accuracy verification method

Many simulated datasets can be used to verify the change detection performance, and the reference images in these datasets are generally binary images, which cannot be used to effectively verify the accuracy of change degree maps in real applications. Therefore, in order to verify the proposed method, a new accuracy verification strategy is proposed.

As shown in Fig.3, high spatial resolution multispectral images of similar time periods are selected as auxiliary data. Compared with hyperspectral data, multispectral data has a small pixel size. For example, when the hyperspectral pixel size is 30 × 30 and that of multispectral image is 10 × 10, a hyperspectral pixel contains nine multispectral pixels. Through the spectral curve of ground objects of the nine multispectral pixels, we can easily know the specific categories and the proportion of each category can be calculated. After that, we can compare the multitemporal change detection result of HS and that of MS, including the composition and change.

III. Experimental Results

3.1 Study area and Experimental data

A. Study area

As show in Fig. 4, to show our methodology and its applicability, the Yellow River Estuary is chosen as our research area. The study area is located at the confluence of Bohai Bay and Laizhou Bay at $118^\circ 10' - 119^\circ 15'$ east longitude and $37^\circ 15' - 38^\circ 10'$ north latitude, Dongying City, Shandong Province, China. This area has a total area of about 9,000 km^2. Due to its spatial geographical location, the study area has formed a complex wetland's ecosystem. The main ground objects include vegetation, water, cultivated land and unused land.

This article has been accepted for publication in a future issue of this journal, but has not been fully edited. Content may change prior to final publication. Citation information: DOI 10.1109/JSTARS.2021.3104164, IEEE Journal of Selected Topics in Applied Earth Observations and Remote Sensing

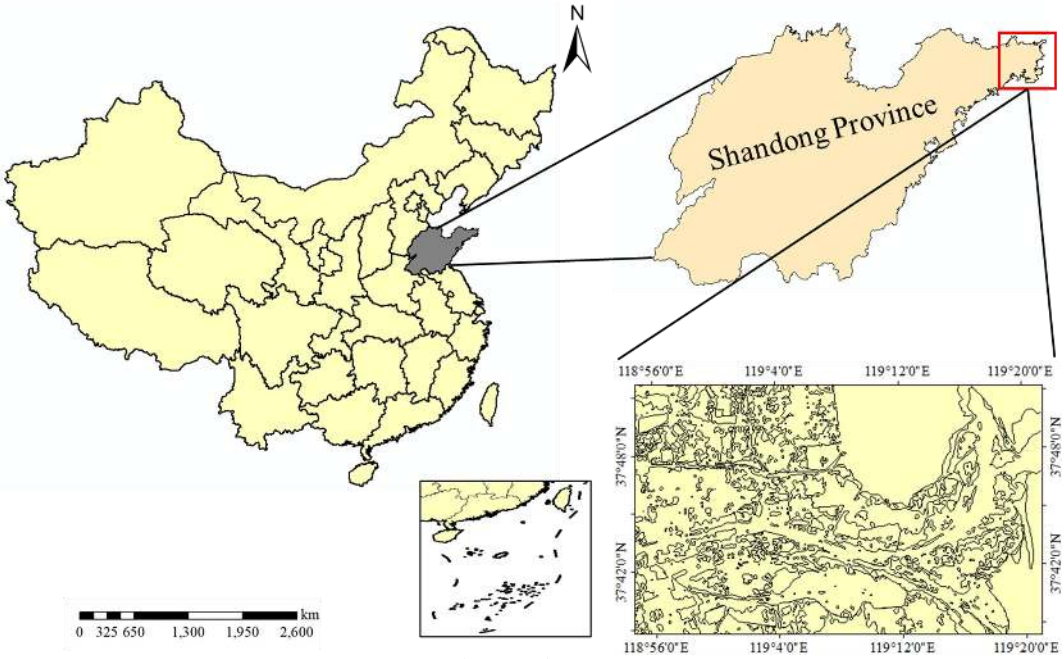

Fig. 4. Study Area.

TABLE I EXPERIMENTAL DATA INFORMATION

	Sensors	GF-5	ZY-1 02D	Sentinel-2A	
Sensor parameters	Nation	China	China	European Space Agency	
	Launch time	2018/05	2019/12	2015/06	
	Orbit altitude (km)	705	738	786	
	Spectral range (nm)	400~2500	400~2500	440~2200	
	Number of bands	330	166	12	
	Spectral resolution (nm)	VNIR: 5 SWIR: 10	VNIR: 10 SWIR: 20	—	
	Spatial resolution (m)	30	30	10/20/60	
	Swath width (km)	60	60	290	
Experimental dataset	Capture time	2018/11/01	2019/12/11	2018/10/24	2019/12/13
	Dimensions	1300*800	1300*800	3900*2400	3900*2400
	Number of bands used	137	137	4	4

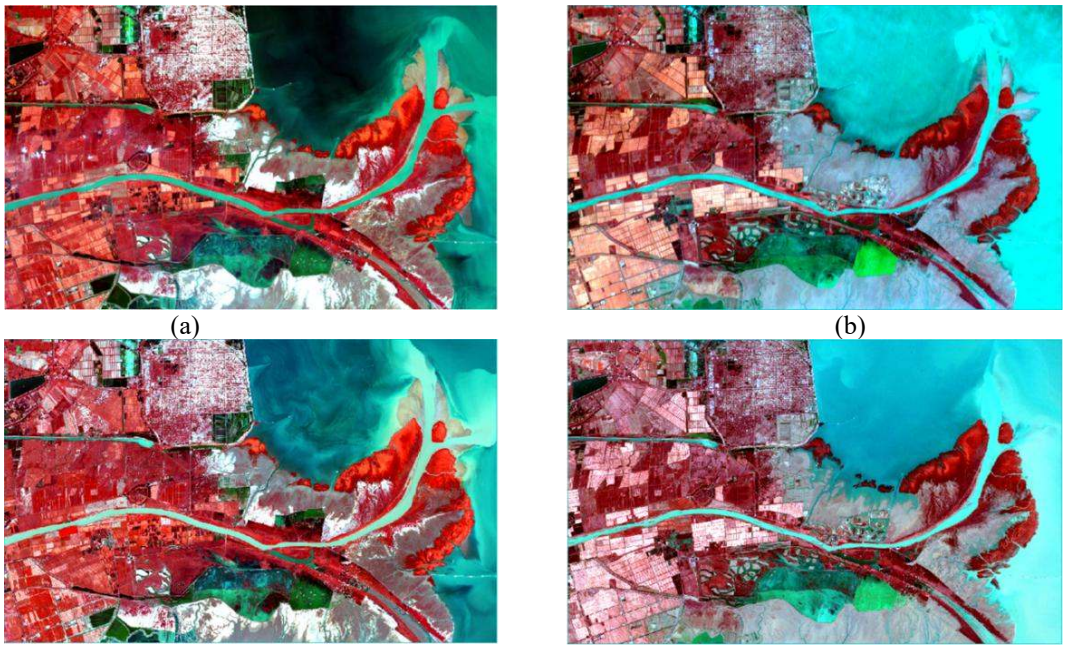

(a) (b) (c) (d)

Fig. 5. Experimental dataset. (a) GF-5-2018.11.1. (b) ZY-1 02D-2019.12.11. (c) Sentinel-2A-2018.10.24. (d) Sentinel-2A-201912.13.

This article has been accepted for publication in a future issue of this journal, but has not been fully edited. Content may change prior to final publication. Citation information: DOI 10.1109/JSTARS.2021.3104164, IEEE Journal of Selected Topics in Applied Earth Observations and Remote Sensing

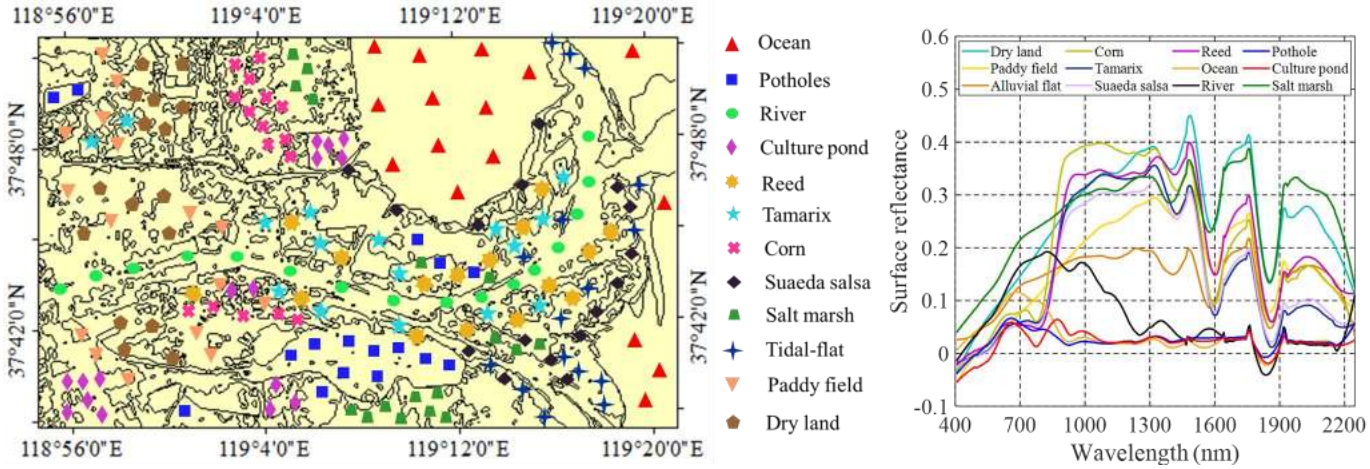

(a) (b)

Fig. 6. Sample distribution map and the mean spectral curves of ground objects.

B. Experimental data

Table I and Fig.5 show the details of the experimental data. We selected GF-5 hyperspectral data (launched in 2018) and ZY-1 02D hyperspectral data (launched in 2019). The GF-5 data was captured on November 1, 2018. It contains 330 bands, with a spectral range of 400-2500 nm, a spatial resolution of 30 m, and a width of 60 km; The ZY-1 02D data, obtained on December 5, 2019, has the same spectral range, spatial resolution and width as the GF-5 data, and only contains 166 bands. To select the common area, the final pixel size of the dataset is 800×1300. In addition, we selected the common or adjacent bands in the two images after removing the bands with severe water vapor absorption in the images, and the final dataset contains a total of 137 bands.

For the validation dataset, we selected the sentinel-2A data which was similar to the capture date of the experimental dataset, and the acquisition time was October 24, 2018 and December 13, 2019, respectively. The validation dataset is multispectral data, including four bands with spatial resolution of 10 m, and the spectral range is 400-900 nm. By selecting the overlapping region, the final image size is 2400 × 3900.

To evaluate the accuracy of the endmembers, we sampled the ground objects in the field [see Fig.6 (a)], obtained 16 spectral curves randomly from multiple directions for each object, and the mean spectral curves of ground objects were obtained in Fig.6(b).

3.2 Data Preprocessing

In the experiment, the dataset was preprocessed firstly, including orthorectification, radiometric calibration, atmospheric correction, geometric correction and image cropping. For the experimental data set, we first converted the images into the WGS1984 coordinate system, the GF-5 and ZY-1 02D hyperspectral data using the global elevation digital model (DEM) of 30 m, and used the rational coefficient file and bilinear interpolation method to perform data resampling.

After that, the gain and offset files were used to calibrate the data, and to perform atmospheric correction by the FLAASH model. Then, we used GF-5 data as the reference image, ZY-1 02D image was spatially registered. It is worth noting that the used geographic control points are global, and the error is controlled within one pixel. Finally, we cropped the same area of the image. For the validation data, we used the same steps to preprocess the data, too.

3.3 Experimental Verification of DSNMF

A. Simulated experimental results

To test our method, we randomly select a group of endmember signals from the USGS spectral library. A linear mixture of different endmembers is constructed to formulate the initial abundance image. Using the traditional K-means clustering method, the initial abundance image is further divided into multiple clusters. After that, a Gaussian filter is applied to generate the abundance ratio of pixels in each cluster partition. The abundance ratio of each pixel satisfies the non-negativity (ANC) and sum-to-one (ASC) constraints [24]. Finally, the zero mean Gaussian noise is added to the synthetic image with different SNRs from 30:1 to 90:1. Fig.7 shows the synthetic hyperspectral image, Fig.8 and Table II show the quantitative results by using SAM [25], spectral information divergence (SID) [26] and correlation coefficient (CC) [27], and our method is compared with Vertex Component Analysis (VCA) [28], N-FINDR [29], Simplex Identification via Split Augmented Lagrangian (SISAL) [30], Non-negative Matrix Factorization (NMF) (NMF) [31].

This article has been accepted for publication in a future issue of this journal, but has not been fully edited. Content may change prior to final publication. Citation information: DOI 10.1109/JSTARS.2021.3104164, IEEE Journal of Selected Topics in Applied Earth Observations and Remote Sensing

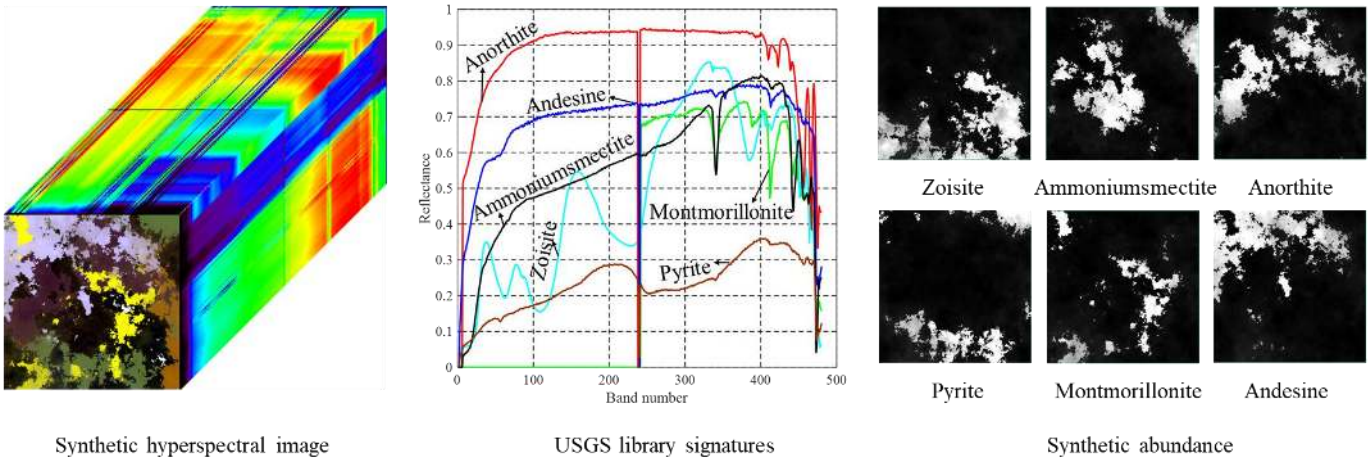

Fig. 7. Simulated data

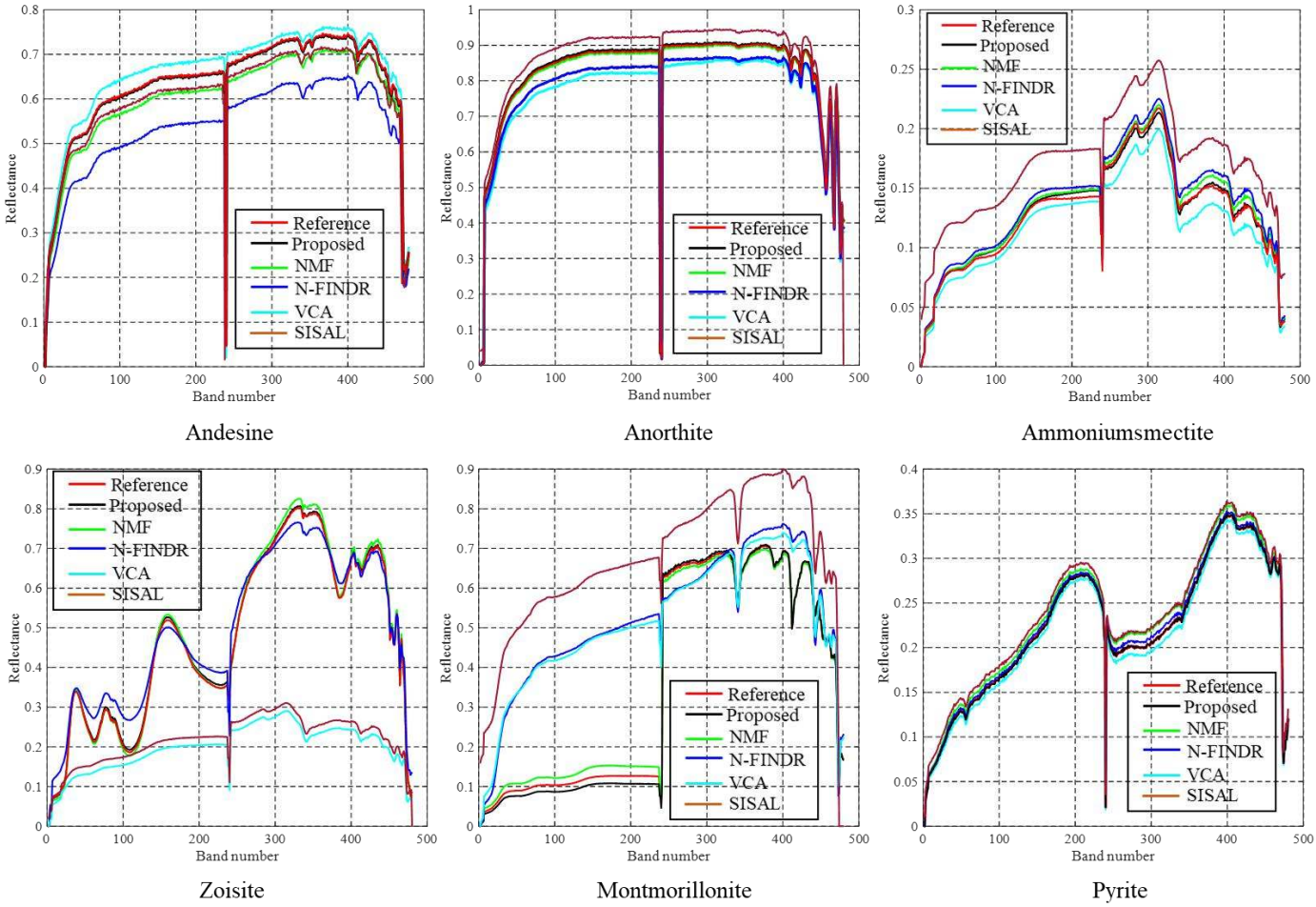

Fig. 8. Comparison results of extracted endmembers

Fig.9 and Table III show the abundance evaluation results of various methods, measured from CC [27], Abundance Information Divergence (AID) [32] and Abundance Angle Distance (AAD) [33]. It is shown that the SUNSAL method has more superior performance than other methods, and it is used for abundance estimation in further experiments.

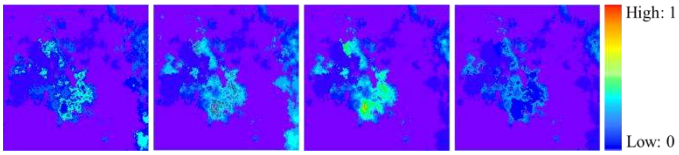

Fig. 9. Error maps of different methods after reconstructing the hyperspectral images

This article has been accepted for publication in a future issue of this journal, but has not been fully edited. Content may change prior to final publication. Citation information: DOI 10.1109/JSTARS.2021.3104164, IEEE Journal of Selected Topics in Applied Earth Observations and Remote Sensing

TABLE II QUANTITATIVE RESULTS OF EXTRACTED ENDMEMBER

Methods		Endmembers					
		Andesine	Anorthite	Ammonium smectite	Zoisite	Montmorillonite	Pyrite
VCA	SAM	0.30	0.26	0.36	0.38	0.31	0.26
	SID	0.025	0.023	0.024	0.044	0.031	0.016
	CC	0.82	0.82	0.85	0.80	0.81	0.88
N-FINDR	SAM	0.34	0.24	0.22	0.38	0.34	0.23
	SID	0.026	0.024	0.019	0.024	0.035	0.020
	CC	0.79	0.85	0.88	0.86	0.85	0.90
SISAL	SAM	0.23	0.28	0.34	0.35	0.40	0.21
	SID	0.019	0.025	0.029	0.039	0.046	0.019
	CC		0.81	0.83	0.82	0.78	0.90
NMF	SAM	0.22	0.18	0.20	0.24	0.20	0.16
	SID	0.015	0.013	0.017	0.020	0.021	0.015
	CC	0.92	0.88	0.90	0.90	0.89	0.92
Proposed	SAM	**0.15**	**0.13**	**0.12**	**0.14**	**0.11**	**0.13**
	SID	**0.012**	**0.009**	**0.014**	**0.013**	**0.019**	**0.013**
	CC	**0.96**	**0.94**	**0.92**	**0.95**	**0.94**	**0.97**

TABLE III QUANTITATIVE RESULTS OF ABUNDANCE ESTIMATION

Methods	FCLS	SCLSU	NMF	SUNSAL
CC	0.93	0.91	0.87	**0.96**
AID	0.016	0.018	0.022	**0.013**
AAD	0.018	0.021	0.034	**0.014**

B. Real experimental results

We compared the spectral curves of ground objects sampled on the spot with the extracted endmembers, and used SAM [25], CC [27] and SID [26] indicators for quantitative evaluation. Fig.10 shows the spectral curve of the endmembers extracted by our strategy, and the reference spectral curve of the ground objects. Table IV shows the quantitative evaluation results of endmembers. The ocean, water bodies, reeds and unused land have achieved good results, followed by potholes and Culture Pond, and tamarisk, suaeda salsa and corn have achieved general evaluation results. The main reason is that the spectral separation between vegetation is very small. In general, the endmembers extracted by our strategy have achieved very high accuracy.

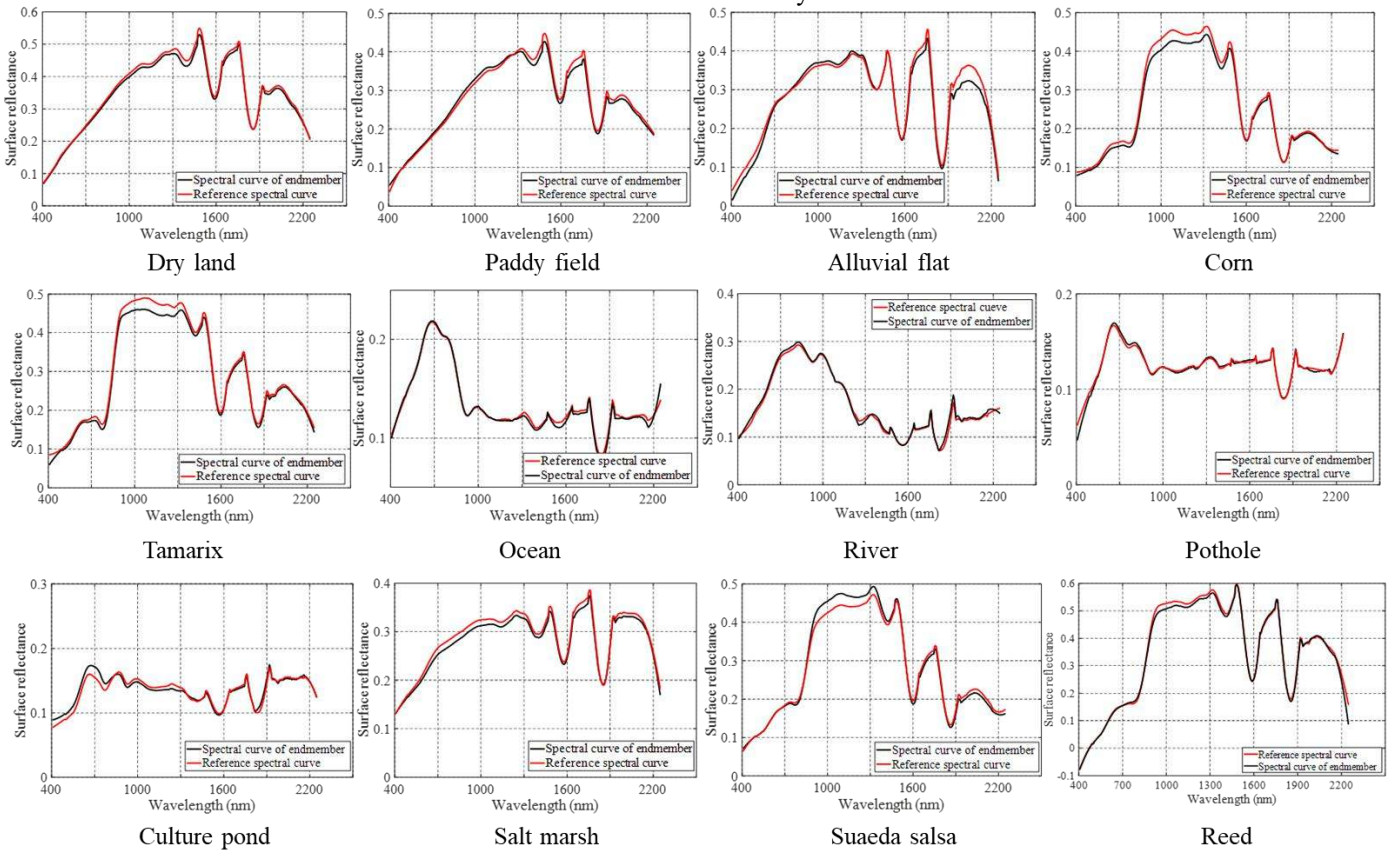

Fig. 10 The comparison results of spectral curves

This article has been accepted for publication in a future issue of this journal, but has not been fully edited. Content may change prior to final publication. Citation information: DOI 10.1109/JSTARS.2021.3104164, IEEE Journal of Selected Topics in Applied Earth Observations and Remote Sensing

TABLE IV COMPARISON RESULTS OF THE ENDMEMBER PURITY

Method	Classes											
	Ocean	Pothole	River	Culture pond	Reed	Tamarix	Corn	Suaeda salsa	Salt marsh	Tidal-flat	Paddy field	Dry land
SAM	0.15	0.19	0.12	0.34	0.31	0.41	0.44	0.33	0.13	0.19	0.13	0.17
CC	0.96	0.94	0.97	0.92	0.93	0.92	0.92	0.93	0.96	0.95	0.96	0.94
SID	0.016	0.028	0.013	0.024	0.025	0.028	0.031	0.028	0.012	0.018	0.013	0.016

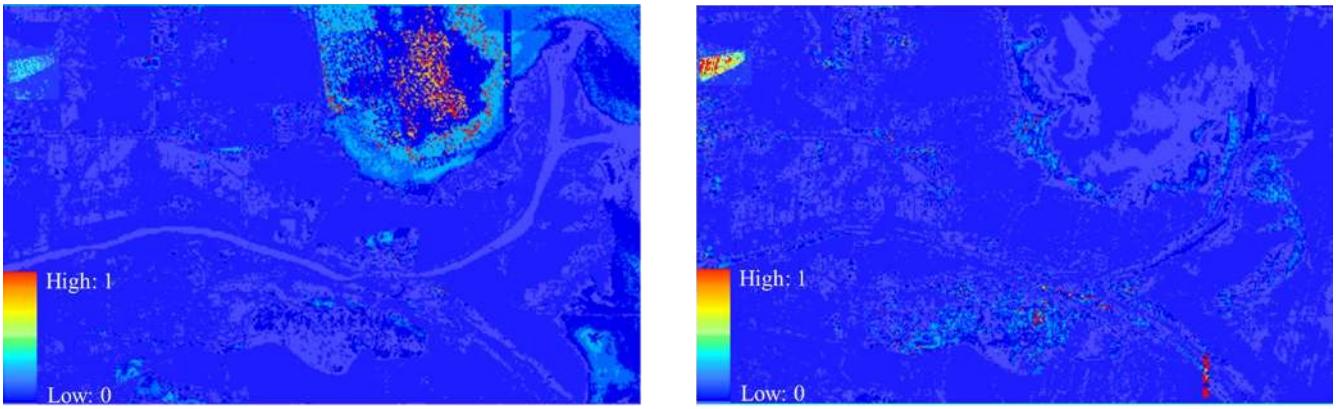

(a) GF-5-2018 (b) ZY-1 02D-2019

Fig. 11. Error maps of multi-temporal hyperspectral images.

We reconstructed the extracted endmembers and abundance, and evaluated the reconstructed image using SAM. Fig.11 shows the SAM map between the reconstructed image and the original image. In general, our method achieves good results, but the error of the reconstructed image in the top-left and down-right is relatively high. We think that the main reason is that 1) the error in the upper right region is that the sea water is mainly affected by light, tide, suspended sediment and microorganism, so that its spectral has variability, leading to some inevitable errors. 2) the top-left error greatly comes from vegetation. When extracting the endmember of sub vegetation, there will be mixed division, and the phenomenon is more serious. This method can distinguish sub vegetation well, but there are still some SAM errors. 3) the spectral signal of unused land is also affected by the external image, and the spectral of salt marsh will also change because of its composition, which has influence on the extraction of its spectral curve.

3.4 Experimental Results of Change Detection

Fig.12 shows the degree of change map and the overall change map obtained by our method. The ocean, salt marshes, and vegetation areas have the most obvious changes, followed by tidal flat areas, and cultivated land and rivers have fewerchanges. We normalized the change degree, and obtained the overall change graph. The white part represents the changed area, and the black part represents the unchanged area. The change mainly exists in the ocean, vegetation and salt marsh area, and the rest of the area has little. Fig.13 shows the abundance estimation results of the image and the component change map of each endmember. The changes of all ground objects were obvious, among which the changes of dry land, alluvial flat, tamarix and reed were the most obvious, the changes of paddy field, corn, potholes, suaeda salsa and ocean were the second, and the changes of river, culture pond and salt marsh were the least.

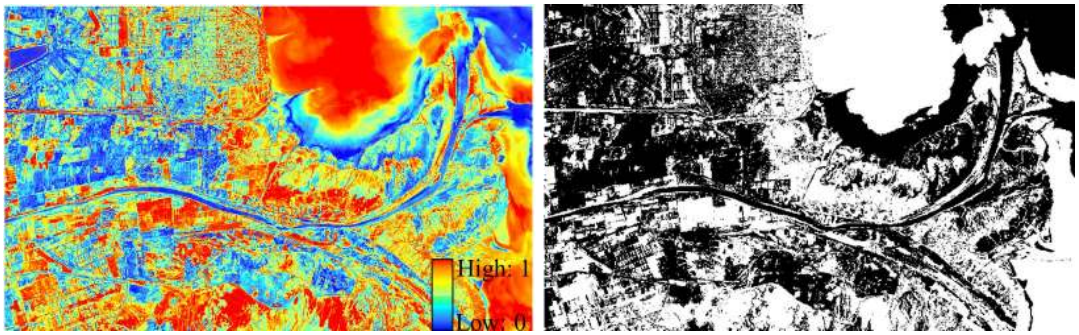

(a) (b)

Fig. 12. Change detection map of the proposed method. (a) Change degree map. (b) Overall change map. (White means change, black means no change).

This article has been accepted for publication in a future issue of this journal, but has not been fully edited. Content may change prior to final publication. Citation information: DOI 10.1109/JSTARS.2021.3104164, IEEE Journal of Selected Topics in Applied Earth Observations and Remote Sensing

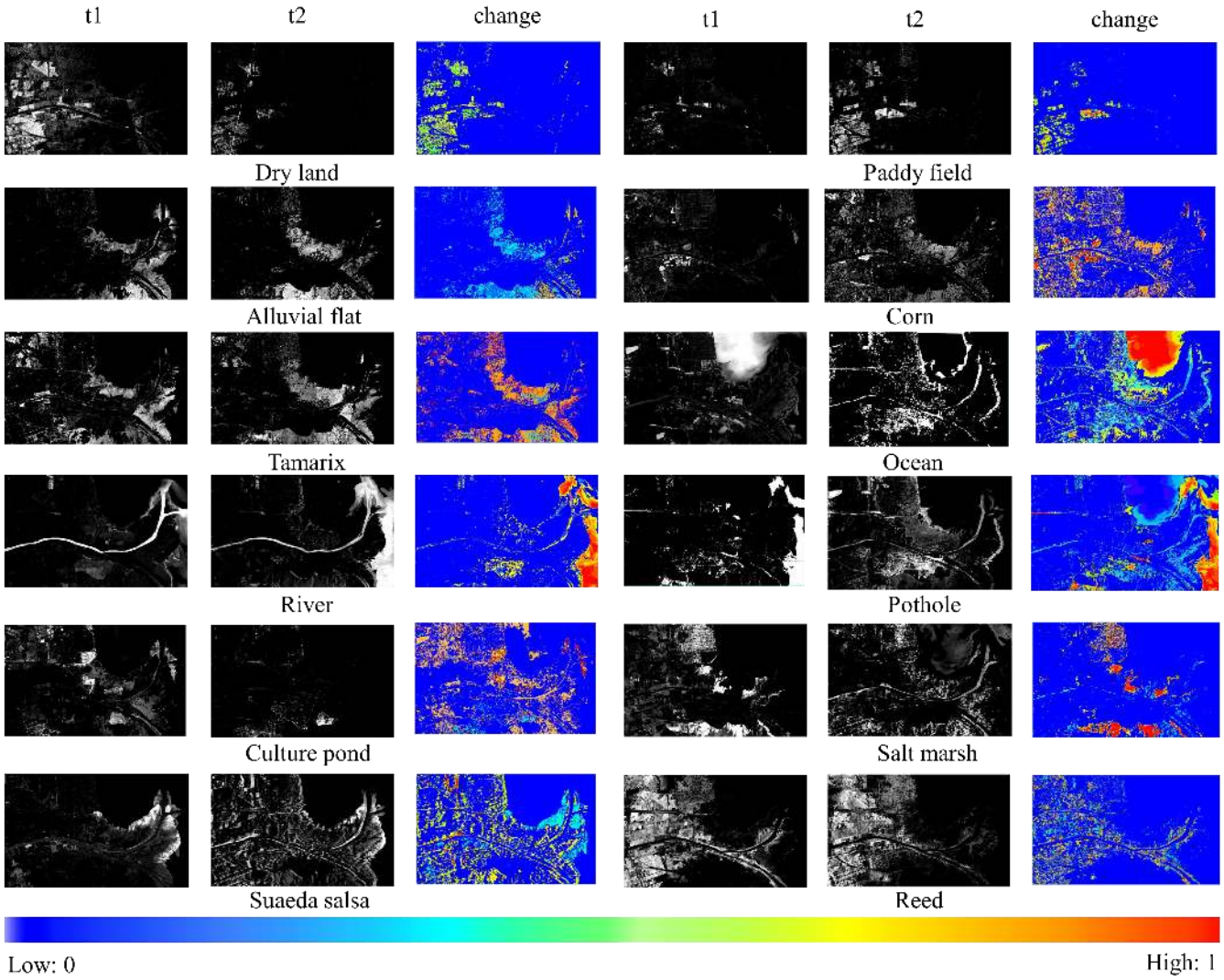

Fig. 13. Abundant estimation results and change graphs.

Fig.14 and Table V - VIII show the verification results of the change detection map from our method. The verification process is mainly developed from four aspects: verification of changes from pure pixels to pure pixels, pure pixels to mixed pixels, mixed pixels to pure pixels, and mixed pixels to mixed pixels. Our method has achieved very good results. Although there are some obvious errors, we argue that the reason of the errors are as follows: 1) We have used multispectral data with a spatial resolution of 10 m for verification. However, due to the lack of spatial resolution, mixed pixels always exist. 2) Although the acquisition time of hyperspectral image and multispectral image is similar, there are still differences in ground objects.

This article has been accepted for publication in a future issue of this journal, but has not been fully edited. Content may change prior to final publication. Citation information: DOI 10.1109/JSTARS.2021.3104164, IEEE Journal of Selected Topics in Applied Earth Observations and Remote Sensing

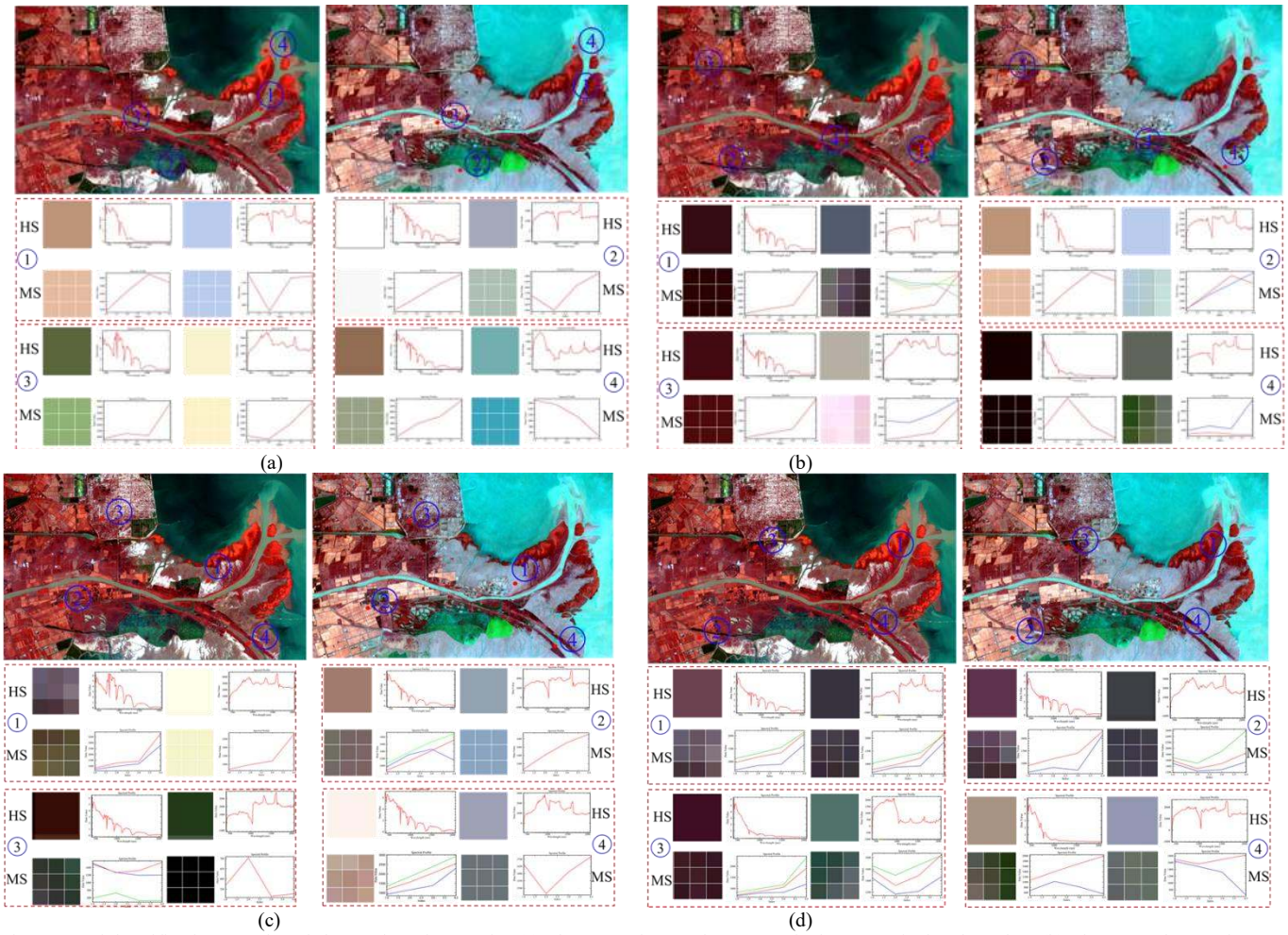

Fig. 14. Partial verification samples of change detection results. (a) The spectral curve from pure pixel to pure pixel endmember. (b) The spectral curve from pure pixel to mixed pixel endmember. (c) The spectral curve from mixed pixel to pure pixel endmember. (d) The spectral curve from mixed pixel to mixed pixel endmember.

TABLE V PURE PIXEL TO PURE PIXEL

Number	Location (Pixel)	Data					
		LRHS			HRMS		
		t1 (%)	*t2* (%)	Change (%)	*t1* (%)	*t2* (%)	Change (%)
EM1	LRHS: (1079, 372) HRMS: (3237, 1116)	River (100)	Alluvial flat (100)	River (-100) Alluvial flat (100)	River (100)	Alluvial flat (100)	River (-100) Alluvial flat (100)
EM2	LRHS: (578, 730) HRMS: (1734, 2190)	Salt marsh (100)	Alluvial flat (100)	Salt marsh (-100) Alluvial flat (100)	Salt marsh (100)	Alluvial flat (100)	Salt marsh (-100) Alluvial flat (100)
EM3	LRHS: (367, 490) HRMS:(1101, 1470)	Paddy field (100)	Dry land (100)	Paddy field (-100) Dry land (100)	Paddy field (100)	Dry land (100)	Paddy field (-100) Dry land (100)
EM4	LRHS: (1046, 137) HRMS: (3138, 411)	Alluvial flat (100)	Ocean (100)	Alluvial flat (-100) Ocean (100)	Alluvial flat (100)	Ocean (100)	Alluvial flat (-100) Ocean (100)
EM5	LRHS: (305, 764) HRMS: (915, 2292)	Pothole (100)	Alluvial flat (100)	Pothole (-100) Alluvial flat (100)	Pothole (100)	Alluvial flat (100)	Pothole (-100) Alluvial flat (100)
EM6	LRHS: (728, 512) HRMS: (2184, 1536)	Reed (100)	River (100)	Reed (-100) River (100)	Reed (89) River (11)	River (100)	Reed (-89) River (89)
EM7	LRHS: (236, 291) HRMS: (708, 873)	Reed (100)	Culture pond (100)	Reed (-100) Culture pond (100)	Reed (78) Culture pond (22)	Culture pond (100)	Reed (-78) Culture pond (78)
EM8	LRHS: (58, 61) HRMS: (174, 183)	Dry land (100)	Corn (100)	Dry land (-100) Corn (100)	Dry land (100)	Corn (100)	Dry land (-100) Corn (100)
EM9	LRHS: (994, 617) HRMS: (2982,	Reed (100)	Alluvial flat (100)	Reed (-100) Alluvial flat (100)	Reed (100)	Alluvial flat (100)	Reed (-100) Alluvial flat (100)

	1851)						
EM10	LRHS: (97, 636) HRMS: (291, 1908)	Paddy field (100)	Dry land (100)	Paddy field (-100) Dry land (100)	Paddy field (89) Dry land (11)	Dry land (100)	Paddy field (-89) Dry land (89)
EM11	LRHS: (461, 509) HRMS: (1383, 1527)	Culture pond (100)	Dry land (100)	Culture pond (-100) Dry land (100)	Culture pond (100)	Dry land (100)	Culture pond (-100) Dry land (100)
EM12	LRHS: (474, 426) HRMS: (1422, 1278)	Reed (100)	Tamarix (100)	Reed (-100) Tamarix (100)	Reed (100)	Tamarix (100)	Reed (-100) Tamarix (100)
EM13	LRHS: (477, 620) HRMS: (1431, 1860)	Reed (100)	Culture pond (100)	Reed (-100) Culture pond (100)	Reed (100)	Culture pond (100)	Reed (-100) Culture pond (100)
EM14	LRHS: (614, 714) HRMS: (1842, 2142)	Tamarix (100)	Pothole (100)	Tamarix (-100) Pothole (100)	Tamarix (89) Pothole (11)	Pothole (100)	Tamarix (-89) Pothole (89)
EM15	LRHS: (308, 685) HRMS: (924, 2055)	Pothole (100)	Salt marsh (100)	Pothole (-100) Salt marsh (100)	Pothole (100)	Salt marsh (100)	Pothole (-100) Salt marsh (100)

TABLE VI PURE PIXEL TO MIXED PIXEL

Number	Location (Pixel)	Data					
		LRHS			HRMS		
		t1 (%)	t2 (%)	Change (%)	t1 (%)	t2 (%)	Change (%)
EM1	LRHS: (702, 526) HRMS: (2106, 1578)	Reed (100)	Salt marsh (20) Reed (29) Alluvial flat (34) River (15) Tamarix (2)	Salt marsh (20) Reed (-71) Alluvial flat (34) River (15) Tamarix (2)	Reed (100)	Salt marsh (23) Reed (33) Alluvial flat (33) River (11)	Salt marsh (23) Reed (67) Alluvial flat (33) River (11)
EM2	LRHS: (1066, 434) HRMS: (3198, 1302)	River (100)	River (40) Alluvial flat (60)	River (-60) Alluvial flat (60)	River (100)	River (33) Alluvial flat (67)	River (-67) Alluvial flat (67)
EM3	LRHS: (350, 506) HRMS:(1050, 1518)	Culture pond (100)	Dry land (50) Tamarix (50)	Culture pond (-100) Dry land (50) Tamarix (50)	Pothole (100)	Dry land (56) Tamarix (44)	Pothole (-100) Dry land (56) Tamarix (44)
EM4	LRHS: (311, 161) HRMS: (933, 483)	Culture pond (100)	Dry land (34) Culture pond (33) Reed (33)	Dry land (34) Culture pond (-67) Reed (33)	Culture pond (100)	Dry land (33) Culture pond (67)	Dry land (33) Culture pond (-33)
EM5	LRHS: (1069, 178) HRMS: (3207, 534)	Alluvial flat (100)	Alluvial flat (83) Ocean (17)	Alluvial flat (-17) Ocean (17)	Alluvial flat (100)	Alluvial flat (78) Ocean (22)	Alluvial flat (-22) Ocean (22)
EM6	LRHS: (61, 63) HRMS: (183, 189)	Dry land (100)	Dry land (62) Tamarix (38)	Dry land (-38) Tamarix (38)	Dry land (100)	Dry land (56) Tamarix (33) Paddy field (11)	Dry land (-44) Tamarix (33) Paddy field (11)
EM7	LRHS: (250, 750) HRMS: (750, 2250)	Tamarix (100)	Dry land (65) Reed (35)	Tamarix (-100) Dry land (65) Reed (35)	Tamarix (100)	Dry land (67) Reed (33)	Tamarix (-100) Dry land (67) Reed (33)
EM8	LRHS: (1082, 227) HRMS: (3246, 681)	Suaeda salsa (100)	Suaeda salsa (64) Reed (36)	Suaeda salsa (-36) Reed (36)	Suaeda salsa (100)	Suaeda salsa (56) Reed (33) Alluvial flat (11)	Suaeda salsa (-44) Reed (33) Alluvial flat (11)
EM9	LRHS: (246, 41) HRMS: (738, 123)	Tamarix (100)	Corn (72) Salt marsh (28)	Tamarix (-100) Corn (72) Salt marsh (28)	Tamarix (100)	Corn (89) Salt marsh (11)	Tamarix (-100) Corn (89) Salt marsh (11)
EM10	LRHS: (217, 74) HRMS: (651, 22)	Dry land (100)	Dry land (61) Reed (30) Salt marsh (9)	Dry land (-39) Reed (30) Salt marsh (9)	Dry land (100)	Dry land (67) Reed (33)	Dry land (-33) Reed (33)
EM11	LRHS: (220, 507) HRMS: (660, 1521)	Dry land (100)	Dry land (42) Reed (17) Salt marsh (18) Culture pond (23)	Dry land (-58) Reed (17) Salt marsh (18) Culture pond (23)	Dry land (100)	Dry land (44) Reed (22) Culture pond (33)	Dry land (-56) Reed (22) Culture pond (33)
EM12	LRHS: (506, 116) HRMS: (1518, 348)	Salt marsh (100)	Salt marsh (50) Tamarix (31) Reed (19)	Salt marsh (-50) Tamarix (31) Reed (19)	Salt marsh (100)	Salt marsh (56) Tamarix (44)	Salt marsh (-44) Tamarix (44)
EM13	LRHS: (633, 577) HRMS: (1899, 1731)	Tamarix (100)	Salt marsh (13) Reed (28) Culture pond (59)	Tamarix (-100) Salt marsh (13) Reed (28) Culture pond (59)	Tamarix (100)	Salt marsh (22) Reed (22) Pothole (56)	Tamarix (-100) Salt marsh (22) Reed (22) Pothole (56)
EM14	LRHS: (399, 646) HRMS: (1197,1938)	Reed (100)	Reed (61) Tamarix (13) Salt marsh (10) Culture pond (16)	Reed (-39) Tamarix (13) Salt marsh (10) Culture pond (16)	Reed (100)	Reed (67) Tamarix (11) Pothole (22)	Reed (-33) Tamarix (11) Pothole (22)

EM15	LRHS: (562, 217) HRMS: (1686, 651)	Culture pond (100)	Culture pond (50) Dry land (37) Salt marsh (13)	Culture pond (-50) Dry land (37) Salt marsh (13)	Pothole (100)	Pothole (67) Dry land (33)	Pothole (-33) Dry land (33)

TABLE VII MIXED PIXEL TO PURE PIXEL

Number	Location (Pixel)	Data					
		LRHS			HRMS		
		t1 (%)	*t2* (%)	Change (%)	*t1* (%)	*t2* (%)	Change (%)
EM1	LRHS: (41, 187) HRMS: (123, 561)	Dry land (25) Reed (42) Tamarix (33)	Dry land (41) Reed (25) Tamarix (34)	Dry land (16) Reed (-17) Tamarix (1)	Dry land (22) Reed (56) Tamarix (22)	Dry land (33) Reed (33) Tamarix (34)	Dry land (11) Reed (-23) Tamarix (12)
EM2	LRHS: (360, 347) HRMS: (1080, 1041)	Reed (63) Tamarix (37)	Salt marsh (35) Pothole (31) Dry land (34)	Reed (-63) Tamarix (-37) Dry land (34) Pothole (31)	Reed (78) Tamarix (22)	Salt marsh (44) Pothole (22) Dry land (33)	Reed (-78) Tamarix (-22) Dry land (33) Pothole (22)
EM3	LRHS: (737, 636) HRMS:(2211, 1908)	Reed (41) Culture pond (34) Tamarix (25)	Reed (56) Culture pond (15) Tamarix (19)	Reed (15) Culture pond (-19) Tamarix (-6)	Reed (33) Pothole (34) Tamarix (33)	Reed (44) Pothole (22) Tamarix (33)	Reed (11) Pothole (-12) Tamarix (0)
EM4	LRHS: (832, 460) HRMS: (2496, 1380)	Reed (44) Pothole (56)	Dry land (21) Salt marsh (79)	Reed (-44) Pothole (-56) Dry land (21) Salt marsh (79)	Reed (56) Culture pond (44)	Dry land (33) Salt marsh (64)	Reed (-56) Culture pond (-44) Dry land (33) Salt marsh (64)
EM5	LRHS: (581, 330) HRMS: (1743, 990)	Suaeda salsa (53) Reed (31) Alluvial flat (16)	Reed (21) Alluvial flat (79)	Suaeda salsa (-53) Reed (10) Alluvial flat (63)	Suaeda salsa (67) Reed (22) Alluvial flat (11)	Reed (33) Alluvial flat (67)	Suaeda salsa (-67) Reed (11) Alluvial flat (56)
EM6	LRHS: (1043, 240) HRMS: (3129, 720)	Ocean (39) Suaeda salsa (14) Alluvial flat (11) Reed (36)	Ocean (31) Alluvial flat (45) Reed (24)	Ocean (-8) Suaeda salsa (-14) Alluvial flat (-34) Reed (12)	Ocean (33) Suaeda salsa (22) Alluvial flat (22) Reed (22)	Ocean (22) Alluvial flat (67) Reed (11)	Ocean (-11) Suaeda salsa (-22) Alluvial flat (45) Reed (-11)
EM7	LRHS: (253, 90) HRMS: (759, 270)	Reed (56) Corn (25) Dry land (19)	Salt marsh (21) Corn (71) Dry land (8)	Reed (-56), Corn (46) Dry land (-11) Salt marsh (21)	Reed (44) Corn (33) Dry land (22)	Salt marsh (33) Corn (56) Dry land (11)	Reed (-44), Corn (23) Dry land (-11) Salt marsh (33)
EM8	LRHS: (100, 464) HRMS: (300, 1392)	Reed (52) Dry land (48)	Salt marsh (40) Dry land (43) Reed (17)	Reed (-35) Dry land (5) Salt marsh (40)	Reed (67) Dry land (33)	Salt marsh (56) Dry land (44)	Reed (-67) Dry land (11) Salt marsh (56)
EM9	LRHS: (591, 474) HRMS: (1773, 1422)	Reed (54) Tamarix (46)	Dry land (64) Pothole (19) Tamarix (17)	Reed (-54),Tamarix (-29) Dry land (64) Pothole (19)	Reed (67) Tamarix (33)	Dry land (78) Pothole (22)	Reed (-67), Tamarix (-33) Dry land (78) Pothole (22)
EM10	LRHS: (204, 764) HRMS: (612, 2292)	Dry land (82) Reed (18)	Dry land (63) Corn (37)	Dry land (-19) Reed (-18) Corn (37)	Dry land (78) Reed (22)	Dry land (56) Corn (33) Salt marsh (11)	Dry land (-22) Reed (-22) Corn (33) Salt marsh (11)
EM11	LRHS: (220, 507) HRMS: (660, 1521)	Dry land (6) Paddy field (49) Salt marsh (45)	Dry land (92) Pothole (8)	Dry land (86) Paddy field (-49) Salt marsh (-45) Pothole (8)	Paddy field (56) Salt marsh (44)	Dry land (89) Pothole (11)	Dry land (89) Paddy field (-56) Salt marsh (-44) Pothole (11)
EM12	LRHS: (106, 18) HRMS: (318, 54)	Reed (83) Tamarix (17)	Reed (15) Salt marsh (85)	Reed (68) Tamarix (-17) Salt marsh (85)	Reed (78) Tamarix (22)	Reed (22) Salt marsh (78)	Reed (56) Tamarix (-22) Salt marsh (78)
EM13	LRHS: (341, 875) HRMS: (1023, 2625)	Salt marsh (66) Dry land (22) Alluvial flat (12)	Dry land (47) Alluvial flat (53)	Salt marsh (-66) Dry land (25) Alluvial flat (41)	Salt marsh (78) Dry land (11) Alluvial flat (11)	Dry land (56) Alluvial flat (44)	Salt marsh (-78) Dry land (45) Alluvial flat (33)
EM14	LRHS: (1056, 614) HRMS: (3168,1842)	Reed (30) Alluvial flat (38) River (32)	Alluvial flat (65) River (35)	Reed (-30) Alluvial flat (27) River (3)	Reed (34) Alluvial flat (33) River (33)	Alluvial flat (67) River (33)	Reed (-34) Alluvial flat (34) River (0)
EM15	LRHS: (536, 249) HRMS: (1608, 747)	Reed (25) Salt marsh (75)	Salt marsh (34) Pothole (66)	Reed (-25) Salt marsh (-41) Pothole (66)	Reed (22) Salt marsh (78)	Salt marsh (44) Pothole (56)	Reed (-22) Salt marsh (-34) Pothole (56)

This article has been accepted for publication in a future issue of this journal, but has not been fully edited. Content may change prior to final publication. Citation information: DOI 10.1109/JSTARS.2021.3104164, IEEE Journal of Selected Topics in Applied Earth Observations and Remote Sensing

TABLE VIII MIXED PIXEL TO MIXED PIXEL

Number	Location (Pixel)	Data					
		LRHS			HRMS		
		t1 (%)	*t2* (%)	Change (%)	*t1* (%)	*t2* (%)	Change (%)
EM1	LRHS: (324, 517) HRMS: (972, 1551)	Dry land (65) Culture pond (35)	Dry land (100)	Dry land (35) Culture pond (-35)	Dry land (78) Culture pond (22)	Dry land (100)	Dry land (22) Culture pond (-22)
EM2	LRHS: (1066, 434) HRMS: (3198, 1302)	Alluvial flat (46) Reed (54)	Alluvial flat (100)	Alluvial flat (54) Reed (-54)	Alluvial flat (33) Reed (44) Salt marsh (23)	Alluvial flat (100)	Alluvial flat (67) Reed (-44) Salt marsh (-23)
EM3	LRHS: (158, 386) HRMS:(474, 1158)	Reed (71) Tamarix (15) Dry land (14)	Dry land (100)	Reed (-71), Tamarix (-15) Dry land (86)	Reed (67) Tamarix (22) Dry land (11)	Dry land (100)	Reed (-67) Tamarix (-22) Dry land (89)
EM4	LRHS: (1053, 512) HRMS: (3159, 1536)	Alluvial flat (40) Reed (54) Salt marsh (6)	Alluvial flat (100)	Alluvial flat (60) Reed (-54) Salt marsh (-6)	Alluvial flat (33) Reed (56) Salt marsh (11)	Alluvial flat (100)	Alluvial flat (67) Reed (-56) Salt marsh (-11)
EM5	LRHS: (367, 474) HRMS: (1101, 1422)	Pothole (53) Paddy field (47)	Dry land (100)	Pothole (-53) Paddy field (-47) Dry land (100)	Pothole (67) Paddy field (33)	Dry land (100)	Pothole (-67) Paddy field (-33) Dry land (100)
EM6	LRHS: (669, 526) HRMS: (2007, 1578)	Reed (81) Tamarix (19)	River (100)	Reed (-81),Tamarix (-19) River (100)	Reed (78) Tamarix (22)	River (100)	Reed (-78),Tamarix (-22) River (100)
EM7	LRHS: (201, 636) HRMS: (603, 1908)	Dry land (51) Paddy field (49)	Dry land (100)	Dry land (49) Paddy field (-49)	Dry land (44) Paddy field (56)	Dry land (100)	Dry land (56) Paddy field (-56)
EM8	LRHS: (360, 172) HRMS: (1080, 516)	Corn (51) Reed (24) Salt marsh (25)	Pothole (100)	Corn (-51), Reed (-24) Salt marsh (-25) Pothole (100)	Corn (67) Reed (33)	Pothole (100)	Corn (-67) Reed (-33) Pothole (100)
EM9	LRHS: (796, 643) HRMS: (2388, 1929)	Reed (42) Tamarix (31) Pothole (27)	Pothole (100)	Reed (-42) Tamarix (-31) Pothole (73)	Reed (33) Tamarix (34) Pothole (33)	Pothole (100)	Reed (-33) Tamarix (-33) Pothole (67)
EM10	LRHS: (1046, 263) HRMS: (3138, 789)	Reed (92) Suaeda salsa (8)	Reed (100)	Reed (8) Suaeda salsa (-8)	Reed (89) Suaeda salsa (11)	Reed (100)	Reed (11) Suaeda salsa (-11)
EM11	LRHS: (360, 731) HRMS: (1080, 2193)	Reed (25) Salt marsh (53) Tamarix (22)	Salt marsh (100)	Reed (-25) Salt marsh (47) Tamarix (-22)	Reed (33) Salt marsh (67)	Salt marsh (100)	Reed (-33) Salt marsh (33)
EM12	LRHS: (357, 487) HRMS: (1071, 1461)	Culture pond (59) Paddy field (31) Pothole (10)	Dry land (100)	Culture pond (-59) Paddy field (-31) Pothole (-10), Dry land (100)	Culture pond (67) Paddy field (33)	Dry land (100)	Culture pond (-67) Paddy field (-33) Dry land (100)
EM13	LRHS: (989, 282) HRMS: (2967, 846)	Alluvial flat (85) Ocean (15)	Ocean (100)	Alluvial flat (-85) Ocean (85)	Alluvial flat (78) Ocean (22)	Ocean (100)	Alluvial flat (-78) Ocean (78)
EM14	LRHS: (38, 216) HRMS: (114,648)	Pothole (68) Corn (32)	Pothole (100)	Pothole (32) Corn (-32)	Pothole (56) Paddy field (33) Corn (11)	Pothole (100)	Pothole (44) Paddy field (-33) Corn (-11)
EM15	LRHS: (679, 448) HRMS: (2037, 1344)	Reed (42) Salt marsh (55) Alluvial flat (3)	Alluvial flat (100)	Reed (-42) Salt marsh (-55) Alluvial flat (97)	Reed (33) Salt marsh (67)	Alluvial flat (100)	Reed (-33) Salt marsh (-67) Alluvial flat (100)

This article has been accepted for publication in a future issue of this journal, but has not been fully edited. Content may change prior to final publication. Citation information: DOI 10.1109/JSTARS.2021.3104164, IEEE Journal of Selected Topics in Applied Earth Observations and Remote Sensing

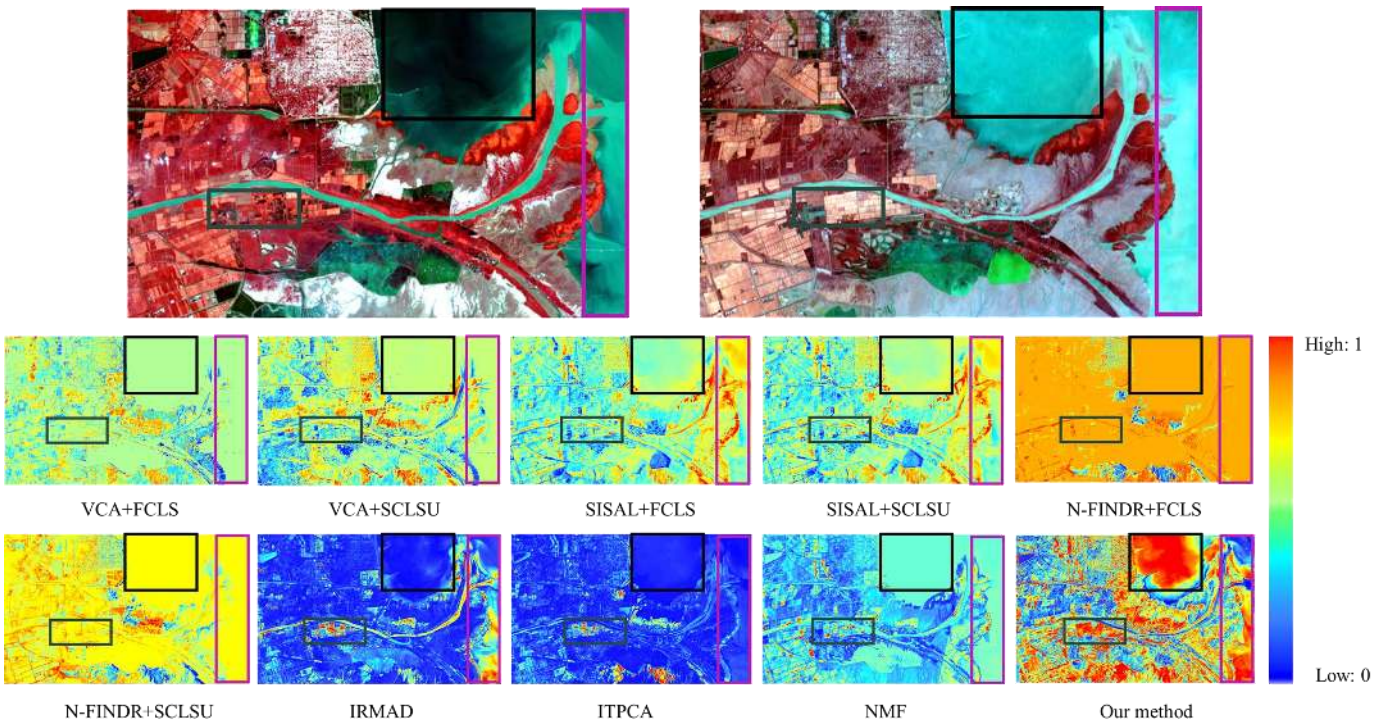

Fig. 15. The comparative results of change degree map from different methods.

The change detection result of SCDUM was compared with nine state-of-the-art methods. The pixel-based methods, IRMAD [11] and ITPCA [10], are selected. Besides, we selected three endmember extraction methods (VCA [28], SISAL [30] and N-FINDR [29]) and two abundance estimation methods (FCLS [23] and SCLSU [22]), and obtained six subpixel-based change detection methods by the combination, including VCA+FCLS, VCA+SCLSU, SISAL+FCLS, SISAL+SCLSU, N-FINDR+FCLS, N-FINDR+SCLSU. DSNMF was also selected to participate in the comparison.

Fig.15 shows the change detection degree map of various methods. According to visual identification, it can be seen that VCA+FCLS, N-FINDR+FCLS and N-FINDR+SCLSU have achieved the worst results; VCA+SCLSU, SISAL+FCLS and SISAL+SCLSU are second, and there are errors in the ocean, dry land, paddy field, reed, salt marshes and other areas; IRMAD, ITPCA and DSNMF have achieved good results. However, significant errors still exist in the ocean, culture pond, potholes and paddy field, and our method achieves the best results.

IV. Discussion

In this paper, we proposed a SCDUM method, which includes the image unmixing and change detection. We presented a novel different spatial scale DSNMF for pure endmember extraction, and a high accurate sub-pixel change detection was obtained based on the proposed SCDUM method. Moreover, the change detection evaluation without reference was designed with the assistance of high spatial resolution MS image.

The proposed SCDUM includes two main parameters, the number of clusters and endmembers. For the number of clusters, we set it to 4: vegetation, water bodies, buildings, and others. It can also be appropriately increased when the local objects are complex. For the number of endmembers, we manually set it based on prior knowledge. VD [25] and Hysime [25] can also be used to estimate the number of endmembers. However, these methods usually overestimate the number of endmembers and degrade the accuracy of change detection.

On the whole, The DSNMF has high computational efficiency, due to the extraction process of initial endmember is performed in low spatial resolution images. Besides, the coupling extraction method of endmember is used to further improve the accuracy of endmember extraction. Most importantly, our method extracts homogeneous regions to make the ground objects have uniformity in space. On this basis, the endmembers are extracted through spectral information. SCDUM makes full use of the spatial-spectral information of the image, and the computational efficiency is high.

The non-reference evaluation of change detection results has always been an urgent problem to be solved, and the evaluation method we proposed can well solve this problem. However, there are some inevitable problems. For example, there is no high spatial resolution data in the same area with similar dates. The study area varies greatly from day to day, and there is a significant difference between the high spatial resolution data and the research data on similar dates. Therefore, no reference evaluation method of change detection results is an important research direction.

V. Conclusion

To the best of our knowledge, this is the first study aimed at detecting the interannual change of the Yellow River Estuary by sub-pixel analysis. In this paper, the SCDUM method and accuracy verification method were proposed. For SCDUM, we firstly mosaiced the multi-temporal images, and clustered and segmented the data by extracting the multiple features of the images. Secondly, we reduced the resolution of all the

segmented images, extracted endmembers from the original spatial scale and down-sampled spatial scale images, and estimated the abundance of the images. Finally, we subtracted the abundance maps of the two phases to get the change map of each endmember, and added the change map of each endmember to obtain the overall change map of the features. For the accuracy verification, we used the high spatial resolution image as the auxiliary data, and compared the endmember change ratio of hyperspectral image with the corresponding proportion of pixels in high spatial resolution image. In this experiment, the Yellow River Estuary wetlands was selected as the research area, and the hyperspectral data of GF-5 and ZY-1 02D were used as the research datasets. Compared with the current mainstream change detection methods and unmixing-based change detection methods, the proposed method can obtain high-quality and high-precision sub-pixel change detection results. Besides, the interannual change of the Yellow River Estuary region is mainly in the human activity area, including cultivated land, potholes and culture ponds. Experimental results show that the wetlands vegetation area has a small change, and the overall change is large in the South and small in the North.

REFERENCE

[1] M. Magdalena and M. Marek, "Wetland Mapping Using SAR Data from the Sentinel-1A and TanDEM-X Missions: A Comparative Study in the Biebrza Floodplain (Poland)," *Remote Sensing,* vol. 10, no. 2, pp. 78-, 2018.

[2] RAMSEY and W. E., "Monitoring flooding in coastal wetlands by using radar imagery and ground-based measurements," *International Journal of Remote Sensing,* vol. 16, no. 13, pp. 2495-2502, 1995.

[3] L. Jiao, W. Sun, G. Yang, G. Ren, and Y. Liu, "A hierarchical classification framework of satellite multispectral/hyperspectral images for mapping coastal wetlands," *Remote Sensing,* vol. 39, no. 20, pp. 1-55, 2018.

[4] J. Peng et al., "Low-Rank and Sparse Representation for Hyperspectral Image Processing: A Review," IEEE Geoscience and Remote Sensing Magazine, vol. 99, no. 1, pp. 2-35, 2021.

[5] Sun W, Ren K, Meng X, et al., "A Band Divide-and-Conquer Multispectral and Hyperspectral Image Fusion Method, "IEEE Transactions on Geoscience and Remote Sensing, pp. 1-13, 2021.

[6] C. Kwan, "Methods and Challenges Using Multispectral and Hyperspectral Images for Practical Change Detection Applications," *Information,* vol. 10, no. 11, p. 353, 2019.

[7] C. Wu, B. Du, and L. Zhang, "Hyperspectral anomalous change detection based on joint sparse representation," *Isprs Journal of Photogrammetry Remote Sensing of Environment,* vol. 146, no. DEC., pp. 137-150, 2018.

[8] E. Reyes, R. J. Abad, J. Diaz, and V. Manian, "Change detection assessment in a tropical forest using multispectral and hyperspectral images," in *IGARSS 2017 - 2017 IEEE International Geoscience and Remote Sensing Symposium*, Fort Worth, Texas USA, 2017.

[9] T. Habib, J. Inglada, G. Mercier, and Chanussot, "Support vectors reduction in SVM algorithm for abrupt change detection," *IEEE Geoscience Remote Sensing Letters,* vol. 6, no. 3, pp. p.606-610, 2009.

[10] V. Kumar, R. Gupta, S. Kaur, and S. Srivastava, "Change Detection on SAR data using PCA Algorithm," *International Journal of Computers Technology,* vol. 4, no. 2, pp. 313-315, 2013.

[11] X. U. Qiangqiang, Z. Liu, Y. Long, and W. Wei, "Change Detection Method Based on Object Oriented IR-MAD," *Remote Sensing Information,* vol. 10, no. 2, 2017.

[12] Alberga and Vito, "Similarity Measures of Remotely Sensed Multi-Sensor Images for Change Detection Applications," *Remote Sensing,* vol. 1, no. 3, pp. 122-143, 2009.

[13] Y. Zheng and J. H. L. Hansen, "Lane-Change Detection from Steering Signal using Spectral Segmentation and Learning-based Classification," *IEEE Transactions on Intelligent Vehicles,* vol. 52, no. 5, pp. 1-1, 2017.

[14] P. Du, S. Liu, J. Xia, and Y. Zhao, "Information fusion techniques for change detection from multi-temporal remote sensing images," *Information Fusion,* vol. 14, no. 1, pp. 19-27, 2013.

[15] C. C. Hsieh, P. F. Hsieh, and C. W. Lin, "Subpixel Change Detection Based on Abundance and Slope Features," in *IEEE International Conference on Geoscience & Remote Sensing Symposium*, Waikoloa Village,USA, 2006.

[16] A. Ertürk, M.-D. Iordache, and A. Plaza, "Sparse Unmixing With Dictionary Pruning for Hyperspectral Change Detection," *IEEE Journal of Selected Topics in Applied Earth Observations and Remote Sensing,* vol. 10, no. 1, pp. 321-330, 2016.

[17] S. Liu, L. Bruzzone, F. Bovolo, and P. Du, "Hierarchical Unsupervised Change Detection in Multitemporal Hyperspectral Images," *IEEE Transactions on Geoscience Remote Sensing,* vol. 53, no. 1, pp. 244-260, 2014.

[18] F. Kizel, M. Shoshany, N. S. Netanyahu, G. Even-Tzur, and J. A. Benediktsson, "A Stepwise Analytical Projected Gradient Descent Search for Hyperspectral Unmixing and Its Code Vectorization," *IEEE Transactions on Geoence Remote Sensing,* vol. 55, no. 9, pp. 4925-4943, 2017.

[19] M. D. Farrell, Jr. and R. M. Mersereau, "On the impact of PCA dimension reduction for hyperspectral detection of difficult targets," *IEEE Geoscience Remote Sensing Letters,* vol. 2, no. 2, pp. 192-195, 2005.

[20] A. Satpathy, X. Jiang, and H. L. Eng, "LBP-Based Edge-Texture Features for Object Recognition," *IEEE Transactions on image Processing,* vol. 23, no. 5, pp. 1953-1964, 2014.

[21] L. N. Meng and Q. R. Han, "An Improved Binarization Method Combined Global Thresholding with Local Thresholding," *Computer Technology Development,* vol. 10, no. 2, pp. 1-10, 2012.

[22] D. Sykas and V. Karathanassi, "Detection of misallocated endmembers through the network based method," in *Hyperspectral Image & Signal Processing: Evolution in Remote Sensing*, Los Angeles,USA, 2010.

[23] L. Zhang, B. Du, and Y. Zhong, "Hybrid Detectors Based on Selective Endmembers," *IEEE Transactions on Geoscience Remote Sensing,* vol. 48, no. 6, pp. 2633-2646, 2010.

[24] X. Xu, J. Li, C. Wu, and A. Plaza, "Regional clustering-based spatial preprocessing for hyperspectral unmixing,"R*emote Sensing of Environment,* vol. 204, no. 5, pp. 333-346, 2018.

[25] K. Ren, W. Sun, X. Meng, G. Yang, and Q. Du,"Fusing China GF-5 Hyperspectral Data with GF-1, GF-2 and Sentinel-2A Multispectral Data: Which Methods Should Be Used?,"*Remote Sensing,* vol. 12, no. 5, pp. 1-19, 2020.

[26] Qian, Y., Jia, S., Zhou, J., Robles-Kelly, and A.," Hyperspectral Unmixing via Sparsity-Constrained Nonnegative Matrix Factorization," *IEEE Transactions on Geoscience Remote Sensing,* vol. 52, no. 12, pp. 1-13, 2011.

[27] G. Vivone, L. Alparone, J. Chanussot, M. Dalla Mura, A. Garzelli, G. A. Licciardi, R. Restaino, and L. Wald, "A Critical Comparison Among Pansharpening Algorithms," *IEEE Transactions on Geoscience and Remote Sensing,* vol. 53, no. 5, pp. 2565-2586, 2015.

[28] C. I. Chang, S. Y. Chen, H. C. Li, H. M. Chen, and C. H. Wen, "Comparative Study and Analysis Among ATGP, VCA, and SGA for Finding Endmembers in Hyperspectral Imagery," *IEEE*

Journal of Selected Topics in Applied Earth Observations Remote Sensing, vol. 9, no. 9, pp. 1-27, 2017.

[29] L. Ji, X. Geng, S. Kang, Y. Zhao, and G. Peng," Modified N-FINDR endmember extraction algorithm for remote-sensing imagery," *International Journal of Remote Sensing,* vol. 36, no. 7-8, pp. 2148-2162, 2015.

[30] J. Sevilla, G. Martín, and J. M. P. Nascimento, "Parallel hyperspectral unmixing method via split augmented lagrangian on GPU," *IEEE Geoscience Remote Sensing Letters,* vol. 13, no. 5, pp. 626-630, 2016.

[31] J. Cao, L. Zhuo, and H. Tao, "An Endmember Initialization Scheme for Nonnegative Matrix Factorization and Its Application in Hyperspectral Unmixing," *Isprs International Journal of Geo Information,* vol. 7, no. 5, pp. 195-, 2018.

[32] J. Peng, Y. Zhou, W. Sun, Q. Du and L. Xia, "Self-Paced Nonnegative Matrix Factorization for Hyperspectral Unmixing," in IEEE Transactions on Geoscience and Remote Sensing, vol. 59, no. 2, pp. 1501-1515, 2021.

[33] A. Halimi, P. Honeine, and J. M. Bioucas-Dias, "Hyperspectral Unmixing in Presence of Endmember Variability, Nonlinearity or Mismodelling Effects," *IEEE Transactions on Image Processing,* vol. 25, no. 10, pp. 4565-4579, 2016